A STEP-FREQUENCY RADAR IMAGING SYSTEM FOR MICROWAVE NONDESTRUCTIVE EVALUATION

W. H. Weedon

Center for Electromagnetics Research and
Department of Electrical and Computer Engineering
Northeastern University, Boston, MA 02115

W. C. Chew and P. E. Mayes

Electromagnetics Laboratory
Department of Electrical and Computer Engineering
University of Illinois, Urbana, IL 61801

1. INTRODUCTION

Microwave nondestructive evaluation (NDE) is slowly becoming a widely accepted method of testing the internal integrity of many materials such as concrete (used in bridges, buildings, dams, tunnels, etc.), asphalt (used in pavements), composite materials, plastics, epoxy, and rubber (used in seals). The main competing technologies with microwave NDE are ultrasound, eddy current, and thermal imaging. Ultrasound is currently by far the most popular NDE method, due to its inherently high resolution, typically on the order of a millimeter. However, ultrasonic waves have trouble penetrating many materials such as concrete, composites, plastics, etc., and usually require a contacting transducer and a wave coupling gel. Microwaves, in contrast, couple very well into these types of materials, and do not require contacting transducers or coupling media. Microwave NDE techniques, when combined with inverse scattering imaging methods, can potentially generate higher resolution images with deeper penetration than the thermal and eddy-current imaging techniques.

Microwave NDE measurement systems may use either a broadband excitation, such as a short-pulse signal, or a narrowband excitation, such as a continuous wave (CW) signal. Broadband scattering data, when available, generally contain much more useful information about an object's internal structure than CW data. For example, a broadband pulse contains range information in the pulse delay, that a single CW magnitude and phase measurement does not contain. This information, when used properly, can be extremely useful for reconstructing the scattering object from the measurement data.

Two competing methods for generating a broadband pulse are the time-domain impulse radar, and step-frequency radar (SFR) [1]. The time-domain impulse radar, as the name implies, transmits a short-time electromagnetic pulse, which scatters off of an object, and is received using either a sampling receiver or an extremely fast A/D converter. In the SFR approach, CW measurements of both magnitude and phase are collected at several closely-spaced frequencies over a broad frequency band of interest. One of the direct advantages of the SFR approach is that a measurement system may be built around a microwave vector network analyzer, with relatively few specialized components.

Other advantages of SFR over impulse radar are the higher signal-to-noise ratio attainable due to narrowband electronics and the avail-

ability of extremely stable signal sources, resulting in increased mea-surement accuracy and stability [1–4]. This allows for the removal of many sources of systematic (non time-varying) measurement error including the frequency-dependent magnitude and phase variations of connectors, transmission lines, directional couplers, amplifiers and an-tennas. The disadvantage of SFR measurement systems, however, is that the data collection time is generally increased. For high-resolution microwave imaging applications, the increased measurement time can often be justified since there will be additional time required to process the data.

The use of a calibration procedure allows for the removal of many sources of pulse distortion in the time-domain data. Standard network analyzer calibration procedures allow for the removal of distortions due to various system components such as connectors, transmission lines, directional couplers and amplifiers. However, an additional calibration step involving the use of calibration targets allows for the removal of pulse distortions due to the effective aperture, phase dispersion, and resonances of the antennas.

Time-domain inverse scattering imaging techniques, [1, 5–10] used in conjunction with SFR data collection, may be used to generate im-ages of the electromagnetic parameters such as the permittivity and conductivity profiles of scattering objects. Both linear diffraction to-mography (DT) algorithms [11–14] and nonlinear inverse scattering algorithms may be used to process the scattering data. Diffraction to-mography takes into account the fact that microwaves, unlike x-rays, do not travel in straight lines. However DT ignores another wave phe-nomenon known as multiple scattering [15]. The only general method to include both the diffracting and multiple scattering effects of the waves in an image reconstruction is to use an iterative nonlinear in-verse scattering algorithm [1, 5–10, 16–21]. Another important advan-tage of nonlinear inverse scattering is that the procedure imposes few constraints on the sensor configuration. Most DT algorithms place se-vere constraints on the sensor configuration, such as the requirement that sensors be separated by a maximum of one half wavelength. Other algorithms are also limited to monostatic measurement configurations.

The results presented in this paper are processed using the distorted-Born iterative method (DBIM) [1, 5–10, 16] and the local shape func-tion (LSF) method [1, 5]. Both the DBIM method and LSF method are nonlinear iterative time-domain inverse scattering algorithms. The

DBIM algorithm reconstructs an image of either the permittivity or conductivity profile of an inhomogeneous scatterer, whereas the LSF method is used to reconstruct metallic scatterers. We have collected experimental data using an array of Vivaldi antennas. The Vivaldi antenna is a flared slotline antenna with a broad bandwidth that operates from 2 to 12 GHz [22, 23]. Reconstructions of various metallic and dielectric scattering objects including metallic rods, glass rods and plastic PVC pipes from real measurement data collected in our laboratory are shown.

2. INVERSE SCATTERING ALGORITHMS

2.1 Distorted-Born Iterative Method (DBIM)

Consider the two-dimensional (2-D) scattering problem illustrated in Figure 1. A line source of current $J_{z,n}(\boldsymbol{r}, t)$ produces the electric field $E_{z,n}(\boldsymbol{r}, t)$ that is scattered by a 2-D cylindrical scatterer. We shall use the subscript n to parameterize the transmitter number, because generally in an inverse scattering measurement there will be multiple transmitter locations. The scatterer is characterized by the permittivity and conductivity profile $\epsilon(\boldsymbol{r}) + \delta\epsilon(\boldsymbol{r})$, $\sigma(\boldsymbol{r}) + \delta\sigma(\boldsymbol{r})$ and exists in an inhomogeneous background medium $\epsilon(\boldsymbol{r})$, $\sigma(\boldsymbol{r})$. That is, the scatterer consists of a perturbation $\delta\epsilon(\boldsymbol{r})$, $\delta\sigma(\boldsymbol{r})$ in the inhomogeneous background. In the formulation that follows, we shall assume that $\delta\epsilon(\boldsymbol{r})$ and $\delta\sigma(\boldsymbol{r})$ are nonzero only within the support volume V of the scatterer. Hence, the permittivity and conductivity everywhere may be written as $\epsilon(\boldsymbol{r}) + \delta\epsilon(\boldsymbol{r})$, $\sigma(\boldsymbol{r}) + \delta\sigma(\boldsymbol{r})$. This is known as the 2-D E_z-polarization or transverse-magnetic (TM) scattering problem in an inhomogeneous background medium.

Since both the line source and scatterer in our model have infinite extent in the $\hat{z}$-direction, and are z-invariant, the electric field will have only a $\hat{z}$-component. The vertical component of electrical field $E_{z,n}(\boldsymbol{r}, t)$ produced by the line source $J_{z,n}(\boldsymbol{r}, t)$ is given as the solution to the scalar wave equation

$$\left[\nabla^2 - \mu_0\epsilon(\boldsymbol{r})\frac{\partial^2}{\partial t^2} - \mu_0\sigma(\boldsymbol{r})\frac{\partial}{\partial t}\right] E_{z,n}(\boldsymbol{r}, t)$$

$$= \mu_0\frac{\partial}{\partial t}J_{z,n}(\boldsymbol{r}, t) + \mu_0\delta\epsilon(\boldsymbol{r})\frac{\partial^2}{\partial t^2}E_{z,n}(\boldsymbol{r}, t) + \mu_0\delta\sigma(\boldsymbol{r})\frac{\partial}{\partial t}E_{z,n}(\boldsymbol{r}, t) \quad (1)$$

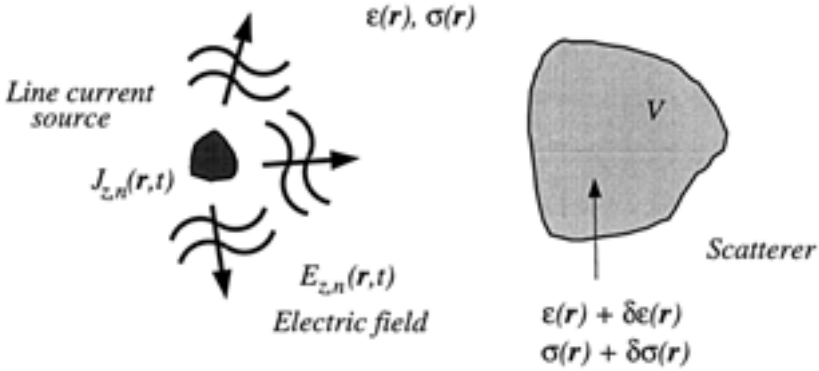Under the distorted Born approximation, the solution to the above

Figure 1. Two-dimensional TM scattering problem where the 2-D scatterer $\delta\epsilon(\boldsymbol{r})$, $\delta\sigma(\boldsymbol{r})$ consists of a perturbation of the background inhomogeneous medium $\epsilon(\boldsymbol{r})$, $\sigma(\boldsymbol{r})$. The scatterer is excited by the $\hat{z}$ directed line source of electric current $J_{z,n}(\boldsymbol{r}, t)$.

partial differential equation (PDE) may be written down as

$$E_{z,n}(\boldsymbol{r}, t) \approx E^0_{z,n}(\boldsymbol{r}, t) + \delta E^\epsilon_{z,n}(\boldsymbol{r}, t) + \delta E^\sigma_{z,n}(\boldsymbol{r}, t). \tag{2}$$

In the above,

$$E^0_{z,n} = -\mu \int_{-\infty}^{\infty} d\boldsymbol{r}' \int_{-\infty}^{\infty} dt' g(\boldsymbol{r}, \boldsymbol{r}') \frac{\partial J_{z,n}(\boldsymbol{r}', t')}{\partial t'} \tag{3}$$

is the incident field in the presence of the background inhomogeneous medium $\epsilon(\boldsymbol{r})$, $\sigma(\boldsymbol{r})$. The terms $\delta E^\epsilon_{z,n}(\boldsymbol{r}, t)$ and $\delta E^\sigma_{z,n}(\boldsymbol{r}, t)$ are the scattered fields induced by the permittivity perturbation $\delta\epsilon(\boldsymbol{r})$ and conductivity perturbation $\delta\sigma(\boldsymbol{r})$ and are given as

$$\delta E^\epsilon_{z,n} = -\mu \int_{-\infty}^{\infty} d\boldsymbol{r}' \int_{-\infty}^{\infty} dt' g(\boldsymbol{r}, \boldsymbol{r}') \delta\epsilon(\boldsymbol{r}') \frac{\partial^2 E^0_{z,n}(\boldsymbol{r}', t')}{\partial t'^2} \tag{4}$$

and

$$\delta E^\epsilon_{z,n} = -\mu \int_{-\infty}^{\infty} d\boldsymbol{r}' \int_{-\infty}^{\infty} dt' g(\boldsymbol{r}, \boldsymbol{r}') \delta\sigma(\boldsymbol{r}') \frac{\partial E^0_{z,n}(\boldsymbol{r}', t')}{\partial t'} \tag{5}$$

The inhomogeneous medium Green's function $g(\boldsymbol{r}, \boldsymbol{r}', t)$ satisfies

$$\left[\nabla^2 - \mu_0\epsilon(\boldsymbol{r})\frac{\partial^2}{\partial t^2} - \mu_0\sigma(\boldsymbol{r})\frac{\partial}{\partial t} \right] g(\boldsymbol{r}, \boldsymbol{r}', t) = -\delta(\boldsymbol{r} - \boldsymbol{r}'). \tag{6}$$

The integral equation given by (2) above is only approximate because the distorted Born approximation [1, 5–7] has been used in writing Equations (4) and (5). The approximation amounts to the fact that the incident field $E_{z,n}^0$ inside integrals in Equations (4) and (5) has been substituted in place of the total field $E_{z,n}$. This approximation is equivalent to assuming that the scattered fields $\delta E_{z,n}^\epsilon$ and $\delta E_{z,n}^\sigma$ are weak compared to the incident field $E_{z,n}^0$ The distorted Born approximation also linearizes the integral equation.

The distorted Born approximation is used frequently in diffraction tomography to perform inverse scattering on objects with weak contrast compared to a known background. But instead of applying the distorted Born approximation only once, this approximation may be applied repeatedly if the background medium is updated at each step. When the distorted Born approximation is used in an iterative fashion, the resulting algorithm is known as the distorted Born iterative method (DBIM). The solution that is obtained from the DBIM solves the nonlinear inverse problem, and hence, is valid for much larger contrasts than if the distorted Born approximation were to be applied only once.

In the DBIM, $\epsilon_k(\boldsymbol{r})$ and $\sigma_k(\boldsymbol{r})$ are the permittivity and conductivity at the kth iteration. $E_{z,n,k}^0$ is the incident field at the kth iteration in the presence of the background medium $\epsilon_k(\boldsymbol{r})$, $\sigma_k(\boldsymbol{r})$ and are computed numerically using a finite-difference time-domain (FDTD) forward solver. The object model parameters $\epsilon_k(\boldsymbol{r})$, $\sigma_k(\boldsymbol{r})$ may be updated at each iteration using an optimization scheme such as the conjugate gradient method.

Equations (4) and (5) above can be thought of as operator forms of the Fréchet derivatives that map perturbations $\delta\epsilon_k(\boldsymbol{r})$ and $\delta\sigma_k(\boldsymbol{r})$ into the field variations $\delta E_{z,n,k}^\epsilon(\boldsymbol{r},t)$ and $\delta E_{z,n,k}^\sigma(\boldsymbol{r},t)$. The Fréchet transposed operators corresponding to these Fréchet derivatives map the field perturbations $\delta E_{z,n,k}^\epsilon(\boldsymbol{r},t)$ and $\delta E_{z,n,k}^\sigma(\boldsymbol{r},t)$ back into the permittivity and conductivity spaces. It can be shown [1, 5–7] that these Fréchet transposed operators are given as

$$\delta\epsilon_k(\boldsymbol{r}) = \mu_0 \sum_{n=1}^{N_T} \int_0^T dt \frac{\partial^2}{\partial t^2} E_{z,n,k}^0(\boldsymbol{r}', T-t) \times \sum_{m=1}^{N_R} \int_0^T dt' g_k(\boldsymbol{r}', \boldsymbol{r}_m, t-t')$$

$$(7)$$

and

$$\delta\sigma_k(\boldsymbol{r}) = \mu_0 \sum_{n=1}^{N_T} \int_0^T dt \frac{\partial}{\partial t} E_{z,n,k}^0(\boldsymbol{r}', T - t) \times \sum_{m=1}^{N_R} \int_0^T dt' g_k(\boldsymbol{r}', \boldsymbol{r}_m, t - t')$$

(8)

Both the Fréchet derivative and transposed operators are required in a conjugate gradient optimization scheme. The Fréchet derivative operator is used in computing the conjugate gradient step size for update along a given search direction and may be computed with a single call to a FDTD forward solver. The Fréchet transposed operator is used to compute the gradient, and hence, the search direction and may be computed as a backpropagation followed by a correlation.

2.2 Local Shape Function (LSF) Method

The DBIM algorithm works well for dielectric and conductive media with contrasts as great as 10:1. But for metallic scatterers, where the contrast is infinite in theory, the linearizing Born approximations that are applied at each step of the DBIM algorithm may not be valid. Recently, we have developed a new inverse scattering method known as the local-shape-function (LSF) method [1, 5] to invert strong metallic scatterers. This technique maps a scatterer with infinite conductivity into a problem with a scatterer described by a binary function which ranges between 0 and 1. By so doing, the extremely nonlinear problem of scattering by a metallic scatterer is mapped into another space where the problem is more linear, but still nonlinear. Eventually, it allows us to iteratively reconstruct metallic scatterers whereas the application of BIM or DBIM would converge extremely slowly or not at all.

Although we have developed LSF theory that applies to both CW and transient excitation, the LSF algorithm is more simply derived in the frequency domain [19, 20]. First, the scattering region is discretized by dividing the scattering volume V into N regions occupying volumes V_i, $i = 1, \ldots, N$. Then, a binary shape function γ_i is assigned to each volume V_i depending on whether the individual volume contains a metallic scatterer. If $\mathcal{S}$ represents the total volume occupied by metallic scatterers, then we have

$$\gamma_i = \begin{cases} 1 & V_i \cap \mathcal{S} \neq 0 \\ 0 & V_i \cap \mathcal{S} = 0 \end{cases}$$
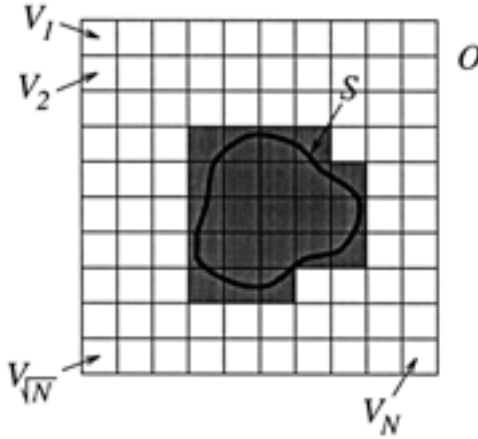
(9)

as in Figure 2.

Figure 2. Discretization of scattering object volume $\mathcal{O}$ into N sub-volumes V_i, $i = 1, \ldots, N$. Surface S indicates the metallic scatterer and the shaded region is where $\gamma_i = 1$.

We now examine how the local shape function may be implemented as a volumetric boundary condition in a FDTD forward solver. Using the FDTD method, a scatterer occupying volume V is discretized into many subvolumes V_i as in Figure 2. We then assume that the scatterer has a homogeneous permittivity and conductivity in each subvolume V_i. Metallic scatterers may be implemented in one of two ways. One method is to simply assign a large conductivity value to the cells where $\gamma_i = 1$. Another way to deal with metallic scatterers is to manually enforce the boundary condition that $E_{z,n}(\boldsymbol{r}_i) = 0$ at the locations $\boldsymbol{r}_i$ where $\gamma_i = 1$. This boundary condition can be thought of as placing a filamental metallic scatterer at each location V_i where $\gamma_i = 1$. We call the above a "volumetric boundary condition" because it is applied at arbitrary locations where $\gamma_i = 1$ inside the volume V.

Mathematically, the LSF volumetric boundary condition may be written as

$$E_{z,n}(\boldsymbol{r}_i, t) = (1 + \gamma_i T_{i(1)}) E_{z,n}^{\mathrm{g}}(\boldsymbol{r}_i, t) \qquad (10)$$

where $T_{i(1)}$ is the single-scatterer T-matrix. In the case of filamental metallic scatterers in a finite difference grid, $T_{i(1)} = -1$. Hence, for $\gamma_i = 1$, Equation (10) enforces the boundary condition $E_{z,n}(\boldsymbol{r}_i, t) = 0$. $E_{z,n}^{\mathrm{g}}(\boldsymbol{r}_i, t)$ is the incident field on the scatterer at position $\boldsymbol{r}_i$ that

includes multiple scattering effects from other cells V_j, $j \neq i$. We call $E_{z,n}^{\mathrm{g}}(\boldsymbol{r}_i, t)$ the "ghost field" because it represents the total field that would be produced at $\boldsymbol{r}_i$ assuming $\gamma_i = 1$, or that a metallic scatterer is not present at $\boldsymbol{r}_i$.

Up to this point, we have assumed that γ_i represents a binary variable that is either 0 or 1. In a practical iterative optimization scheme, it is necessary to relax this requirement and instead let γ_i be a continuous real variable on the interval $[0, 1]$. The inverse scattering algorithm would then produce an image of the variable γ_i as a function of 2-D space.

For brevity, we shall not include the details of the T-matrix formulation of the LSF algorithm here, but rather refer the reader to the literature [1, 5]. The time-domain LSF algorithm may be implemented in an iterative algorithm with a structure similar to that of the DBIM algorithm. The major difference between the new LSF algorithm and the DBIM algorithm is that the Fréchet derivative and Fréchet transposed operators are different.

Using the LSF method the Fréchet derivative operator may be written as

$$\delta E_{z,n,k}(\boldsymbol{r}, t) = \int_{-\infty}^{\infty} d\boldsymbol{r}' \int_0^T dt' h(\boldsymbol{r}, \boldsymbol{r}', t - t') \delta \gamma_k(\boldsymbol{r}') \tag{11}$$

where $h(\boldsymbol{r}, \boldsymbol{r}', t)$ is the inhomogeneous medium Green's function in the presence of $\gamma_k(\boldsymbol{r})$. The Fréchet transposed operator may be written as

$$\delta \gamma_k(\boldsymbol{r}') = \sum_{n=1}^{N_T} \int_0^T dt E_{z,n}^{\mathrm{g}}(\boldsymbol{r}', T - t)$$
$$\times \sum_{m=1}^{N_R} \int_0^T dt' h(\boldsymbol{r}', \boldsymbol{r}_m, t - t') \delta E_{z,n,k}(\boldsymbol{r}_m, T - t') \tag{12}$$

In the integral form of the Fréchet derivative and transposed operators above, we have generalized our definition of the local shape function γ_i to be a function of the continuous variable $\boldsymbol{r}$.

2.3 Measurement Data Processing

Both the DBIM and LSF inverse scattering imaging techniques have been discussed extensively in the past, and their formulation will not

be repeated here. However, for the purposes of completeness, we will give a functional description of the algorithms.

The various steps in the data processing of the measurement data using both the DBIM and LSF algorithms are summarized in the flow diagram of Figure 3. The switch on the left indicates that either measured data or computer generated scattering data (synthetic data) may be used in the inverse scattering algorithm. The algorithm begins with specification of the initial parameters, which are set to zero because we wish to use a minimal amount of a priori information. Using the current computer model, forward scattering data are generated and subtracted from the measured data. This difference is then used to compute a measure of the residual field error. If the difference is below a specified tolerance, the current model parameters are displayed on a graphics workstation. If the field error is not below a specified tolerance, the field error is sent to a conjugate gradient optimization procedure which returns an update to the model parameters. The process is repeated until a convergent solution is attained.

3. MICROWAVE MEASUREMENT APPARATUS

3.1 Description of the SFR System

A block diagram of basic components of the prototype step-frequency radar measurement apparatus is shown in Figure 4. The system consists of a broadband switched antenna array, an HP 8510B automated network analyzer, microwave switches and controller, and an optional broadband amplifier. The entire measurement system is automated and controlled by a computer workstation. Custom software was written in the C programming language to control the measurement apparatus via an IEEE-488 (GPIB) interface. The HP 8510B automated network analyzer serves as both the transmitter and receiver and allows us to collect both amplitude and phase information by stepping through various frequencies.

3.2 Broadband Switched Antenna Array

The broadband switched antenna array used to perform the scattering measurements, shown in Figure 5 contains 11 identically fabricated 2–12 GHz tapered slotline, or Vivaldi, antennas arranged in a linear array, and two DC-18 GHz SP6T microwave switches that are
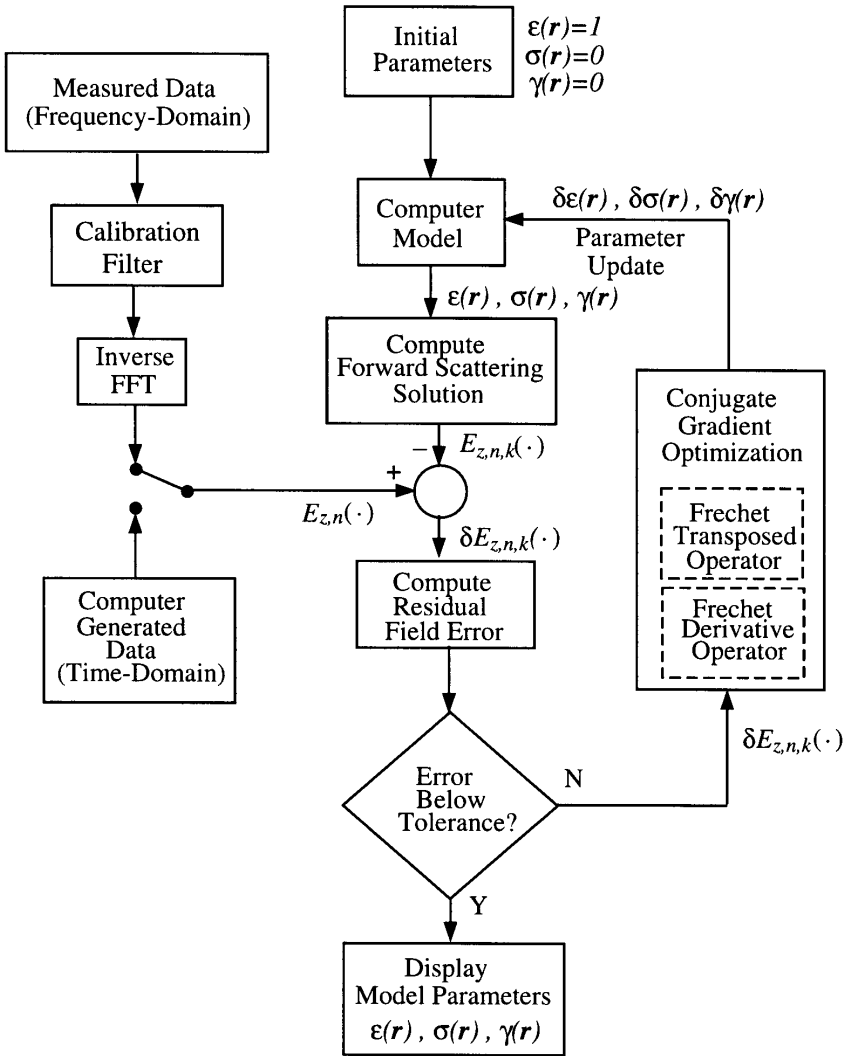
Figure 3. Block diagram of processing of measured and computer simulated scattering data.
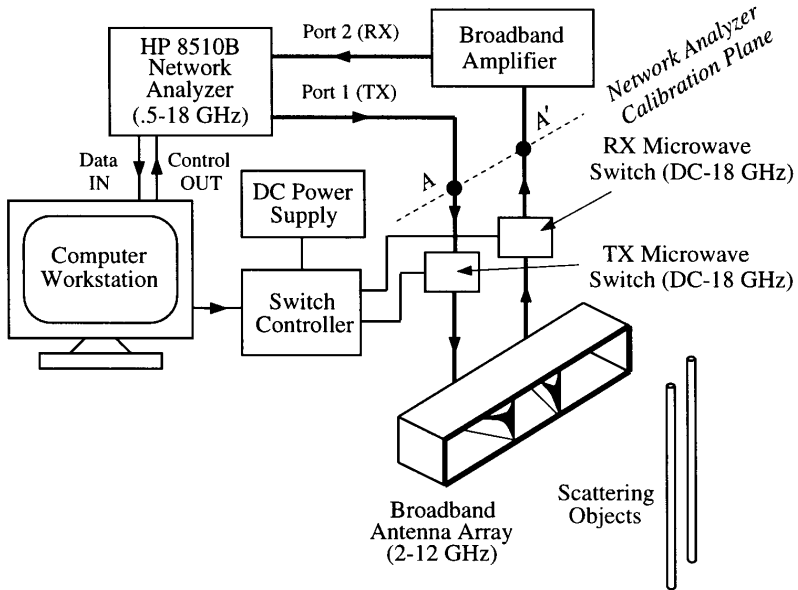
Figure 4. Block diagram of prototype step-frequency radar (SFR) broadband inverse scattering measurement system.

computer controlled. One switch is connected to 5 array elements while 6 elements are connected to the other. Hence, the array may be configured via computer control to operate as either an 11-element monostatic array or a multi-bistatic array consisting of 30 different measurements. The switches automatically terminate the antenna elements at $50\,\Omega$ when they are switched off, reducing the coupling among the elements. The antenna elements and microwave switches are enclosed in a polystyrene housing.

The arrangement of the transmitters and receivers for the new switched antenna array is shown in Figure 6. The 11 antenna elements are separated by $8.0\,\mathrm{cm}$, giving a total baseline of $80.0\,\mathrm{cm}$. This baseline length was chosen with the goal in mind of resolving objects at a range of $R = 40.0\,\mathrm{cm}$. Note in Figure 6 that the antenna elements are aimed at a fixed range of $R = 40.0\,\mathrm{cm}$, rather than straight ahead, in order to achieve the maximum response from all antenna elements at that range.
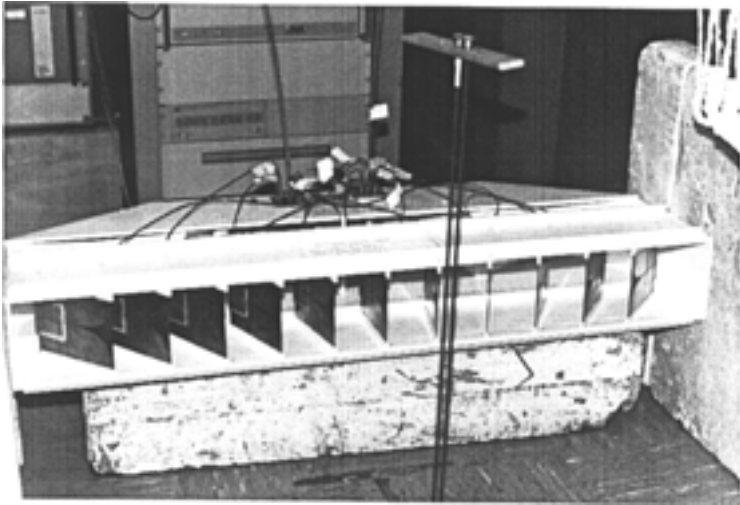
Figure 5. Photograph of broadband switched antenna array containing 11 identical broadband Vivaldi antennas and two microwave switches enclosed in a polystyrene housing.
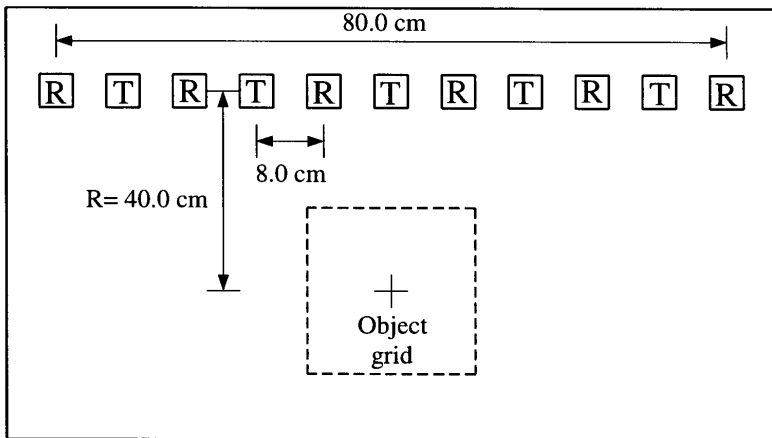

Figure 6. Arrangement of transmitters (T), receivers (R) and object grid for new switched antenna array.

3.3 The Vivaldi Antennas

The Vivaldi antenna is based on a non-resonant travelling-wave structure similar to the horn antenna [24], but is fabricated as a printed circuit antenna. The wave-guiding structure here is the printed slot-line. As in a horn antenna, the waveguide is of increasing dimension, where the increasing dimension is the width of a printed slotline. The names "flared slot" and "tapered notch" have been used for this type of antenna. However, the shorter, but less descriptive, name "Vivaldi antenna" was applied by Gibson [22] to the antenna with exponentially varying separation. The Vivaldi has good potential for applications that require broadband endfire radiation from elements embedded in a truncated ground plane.

The simplicity and excellent performance of the Vivaldi antennas have provoked considerable interest [25]. Though broad bandwidths for the Vivaldi have been documented, the antenna is capable of a wider impedance bandwidth than is usually obtained in practice. Usually, it is the manner of excitation of the Vivaldi slotline that limits the bandwidth rather than the geometry of the flare. Bandwidths greater than 10:1 can be obtained by using a coax-to-slotline (C/S) transition rather than a microstrip-to-slotline used frequently in the past [23]. The method of excitation used in this work is shown in Figure 7. The slotline is etched on both sides of a double-clad substrate. Using double-clad, rather than single-clad, board reduces the characteristic impedance of the slotline for easier matching to a coaxial cable input. Two metallic wedges are affixed to each side of the cladding in such a manner to maintain the width of the slot. The coaxial cable is introduced near the thick edge of the wedges. The thick-walled slot in the neighborhood of the coax is designed for 50-ohm impedance to match that of the coax. The wedge then forms a tapered transition between the relatively low impedance of the coax to the higher impedance of the slotline. Beyond the wedge the slotline is flared exponentially in the manner shown in Figure 7. The resulting antenna structure is well matched to 50-ohms from 1 to beyond 18 GHz. Pattern measurements were limited to 2 to 18 GHz because of range limitations. Well-formed beams were observed over the entire band for both H-plane and E-plane. Cross polarized fields were 20 dB below co-polarized for all of the H-plane data and 15 dB or more for the E-plane data. The measurements confirmed a pattern bandwidth of at least 9:1.
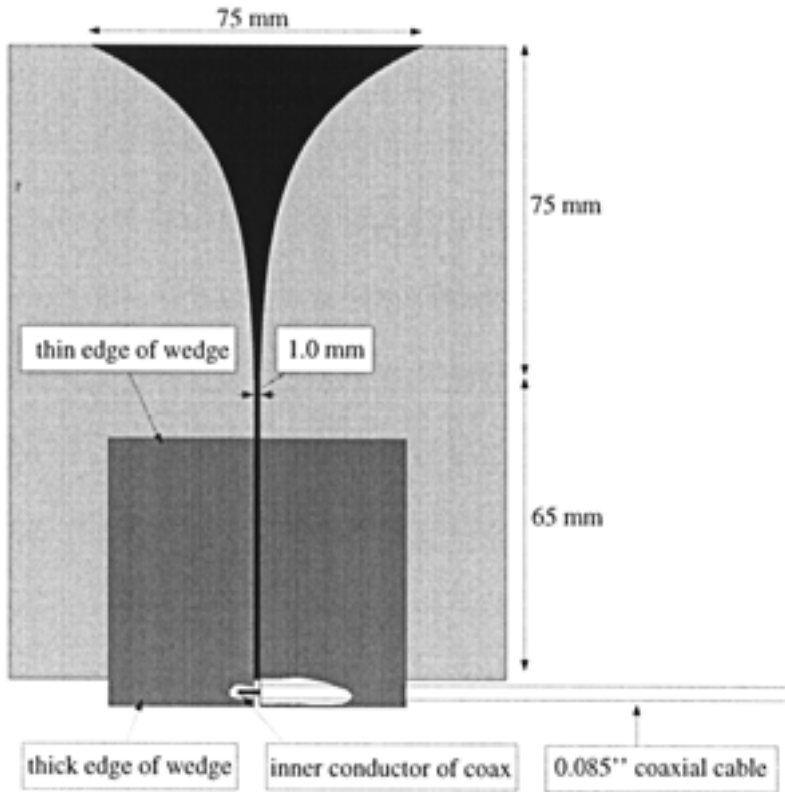
Figure 7. Schematic of the Vivaldi antenna. The black area indicates exposed dielectric substrate. The light gray area indicates copper cladding of the dielectric substrate which occurs on both sides. The dark gray area is the tapered wedge for matching the 50 ohm coaxial cable to the high impedance of the slotline. This antenna consists of a flared slotline.

4. MEASUREMENT CALIBRATION PROCEDURE

For radar imaging applications, distortions of the radar pulse induced by the presence of scatterers can provide much information about the unknown scatterers or targets. That is, much more information may be derived from the shape of the reflected pulse than from the amplitude and arrival time of the pulse alone. But this requires a calibration procedure to remove pulse distortions due to the antennas,

in addition to those distortions normally associated with the network analyzer, including connectors, transmission lines, amplifiers and directional couplers. Fortunately, these distortions may be removed easily in a step-frequency radar system through the use of calibration targets and software.

We will assume that a standard network analyzer calibration procedure is performed so that the analyzer is calibrated to the plane $A - A'$ shown in Figure 4. This calibration would remove the effects of the broadband amplifier, directional couplers, and any transmission lines and connectors between the network analyzer and plane $A - A'$. Hence, if the terminals $A - A'$ were to be shorted together, an S_{21} (transmission) measurement would measure an S_{21} magnitude of $0\,\mathrm{dB}$ and phase of zero degrees for all frequencies.

Next, a procedure involving the use of a calibration target is used to remove the distortions due to the antennas. For this antenna calibration procedure, we shall consider everything from the plane $A - A'$ out to the antennas, including the microwave switches and transmission lines feeding the antennas, to be part of the antenna assembly. Pulse distortions induced by the antenna housing and the presence of the other antenna elements shall also be included in this calibration.

After the standard network analyzer calibration procedure is performed to the plane $A - A'$, the SFR measurement model is as shown in Figure 8(a). A sequence of CW signals in the the bandpass region of interest, taken to be $\omega_L < \omega < \omega_H$, is sent through the transmitting antenna, propagated to the scatterer, and returned to the receiving antenna. The measured field is then inverse Fourier transformed to generate a synthetic scattered field pulse.

To calibrate the antenna array, the scattered field is also computed using a 2-D finite-difference time-domain (FDTD) forward solver. The simulated experiment using the FDTD solution may be modeled as shown in Figure 8(b). The FDTD algorithm models the antennas as line sources of electric current $J_z(\boldsymbol{r}_n, t)$, where $\boldsymbol{r}_n$, $n = 1, 2, \ldots, N$ denotes the nth source location. The wave propagation process is simulated using FDTD and the field is sampled at the receiver locations $\boldsymbol{r}_m$, $m = 1, 2, \ldots, M$.

The purpose of our calibration procedure is to get the measured scattered field pulse to agree with the FDTD model. Since the FDTD forward solver is used extensively in our inverse scattering algorithms, the SFR measurement should agree with the FDTD solution for known
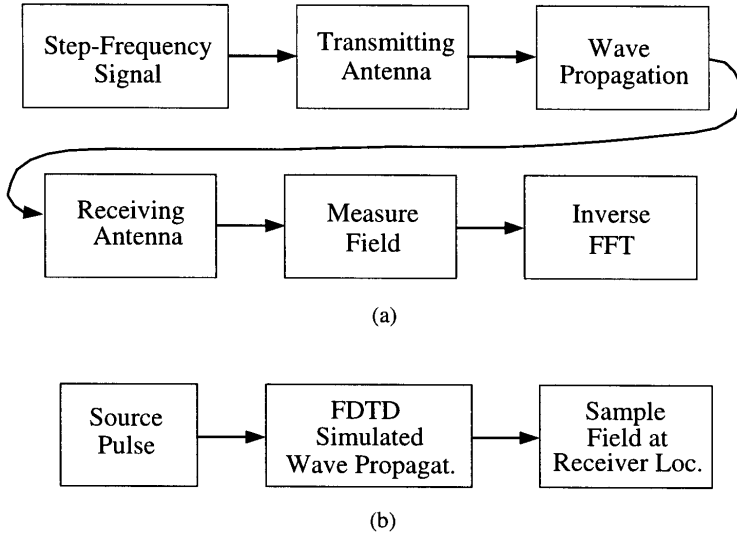
(a)

(b)

Figure 8. (a) Step-frequency radar measurement model and (b) FDTD computer model of scattering experiment.

scatterers. A linear filter $H(\omega)$ is derived as

$$H(\omega) = \begin{cases} \frac{H_c(\omega)}{H_m(\omega)}, & \omega_L < \omega < \omega_H \\ 0, & \text{elsewise}, \end{cases}$$

where $H_c(\omega)$ is the Fourier transform of the computed scattered field obtained from the FDTD simulation of the calibration target and $H_m(\omega)$ is obtained from the raw SFR measurements from the calibration target. The calibration filter $H(\omega)$ is applied to all of the measured SFR data, when the calibration target is replaced with an unknown scatterer. The calibration filter essentially deconvolves the impulse response of the transmitting and receiving antennas, and convolves the FDTD source pulse with the measured data.

The FDTD source pulse is designed in the frequency domain using a Kaiser frequency window and chosen to be relatively constant over the passband $\omega_L < \omega < \omega_H$, but to have a very small amplitude at the band edges ω_L and ω_H. This ensures that $H_c(\omega)$ and $H(\omega)$ will have very small amplitude at the band edges. There is no problem then in specifying the filter $H(\omega)$ to be zero outside the passband.

The 2-D FDTD simulation attempts to predict the ideal scattered field, that is, the scattered field that would be measured with an SFR system if antenna distortions and other sources of modeling error and noise were not present. In the process, however, additional sources of error are introduced. An obvious source of modeling error introduced is the approximation of the 3-D scattering experiment using a 2-D computer model. Another source of modeling error is the representation of the antennas as omni-directional. In actuality, the near-field antenna response varies with both range and angle, in addition to frequency. Numerical noise is also introduced by the FDTD simulation.

For an object region that is small with respect to the size of the array and remains at a fixed location with respect to the array, the two sources of FDTD modeling error discussed above remain relatively constant over the object grid. The calibration procedure then may be considered to be valid within a localized region around the center of the object grid. For object regions that are not small with respect to the size of the array, a more sophisticated calibration procedure may be devised using multiple calibration targets.

5. RESULTS

5.1 Calibration Results

The SFR antenna calibration was performed using a metallic cylinder of diameter 3.0 cm as a calibration target. To demonstrate the effectiveness of the calibration procedure, the calibration target was replaced with an arbitrary target consisting of two metallic cylinders, each of diameter 4.5 mm, separated by 3.2 cm, and aligned vertically with respect to the array.

Figure 9 shows the calibrated time-domain scattering data obtained from the SFR measurements. The scattered field computed using the 2-D FDTD solver is shown in Figure 10. Note that In Figures 9 and 10, only the scattering data for the first transmitter is shown, with the received signal at each of the six receivers. A comparison of Figures 9 and 10 shows that the calibration does an excellent job of getting the measured pulse shape to agree with the pulse calculated with the FDTD algorithm.
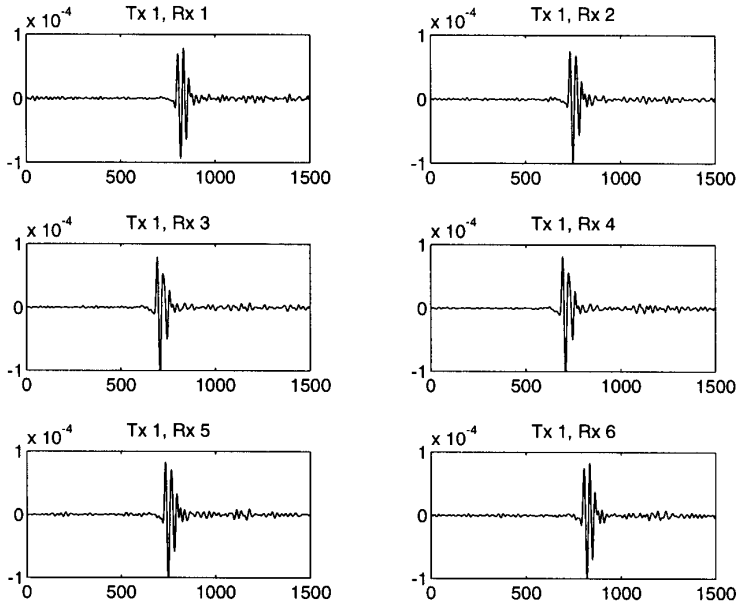
Figure 9. Calibrated time-domain scattering data for two metallic cylinders aligned vertically, obtained from the SFR measurements. Cylinders each have diameter of $4.5\,\mathrm{mm}$ and are separated by $3.2\,\mathrm{cm}$. Data is shown for the first transmitter only and all six receivers.

5.2 Metallic Object Reconstructions

The measurement geometry used in the SFR data collection is shown in Figure 3. The object space consisted of a 35×35 subgrid. The grid space and time step sizes used in the FDTD forward solver were $\Delta x = 2.5\,\mathrm{mm}$ and $\Delta t = 5.5\,\mathrm{ps}$.

Figures 11 and 12 show the resulting images after the LSF inverse scattering algorithm was applied to the measured scattering data from two metallic cylinders. Figure 11 is for the case when the cylinders were aligned horizontally with respect to the array, and Figure 12 is for the vertical alignment case. In both cases, the cylinders were separated by $3.2\,\mathrm{cm}$, and the cylinders each had a diameter of $4.5\,\mathrm{mm}$.
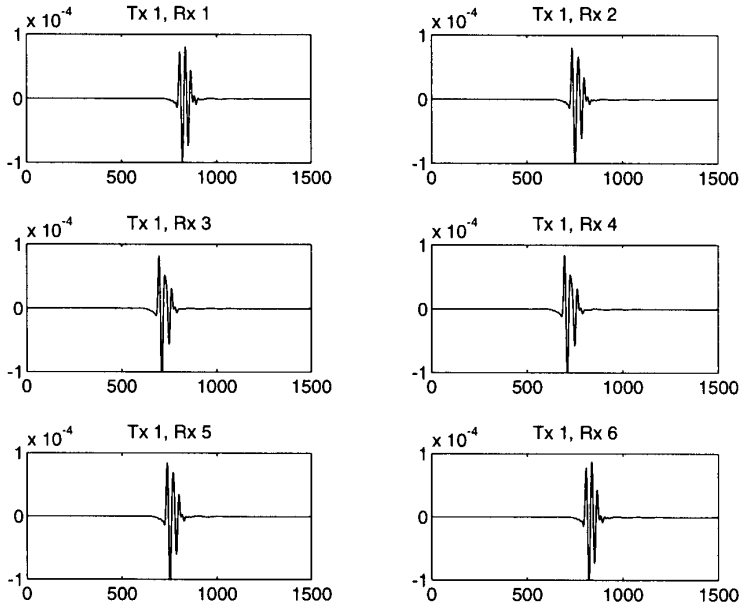
Figure 10. Scattered field computed using finite-difference time-domain for two metallic cylinders aligned vertically. Cylinders each have diameter of 4.5 mm and are separated by 3.2 cm.

5.3 Dielectric Object Reconstructions

Metallic objects are more difficult for inverse scattering algorithms to image than dielectric objects because the inverse scattering problem is more nonlinear for metallic objects. However, dielectric objects are more difficult to measure because the scattered field produced by a dielectric object is much weaker than that of a metallic object. We present reconstructions of dielectric objects below to demonstrate that accurate scattering data can be collected from dielectric objects and that high-quality images may be generated.

Figures 13 and 14 show reconstructions of plastic PVC pipes of diameters 2.7 cm and 4.8 cm, respectively. Both of these pipes were located in an air background. The DBIM permittivity optimization algorithm was used for both cases. For both pipes, high quality images were produced. The bottoms of the pipes are not reconstructed as well as the tops because scattering data were collected from the top only.
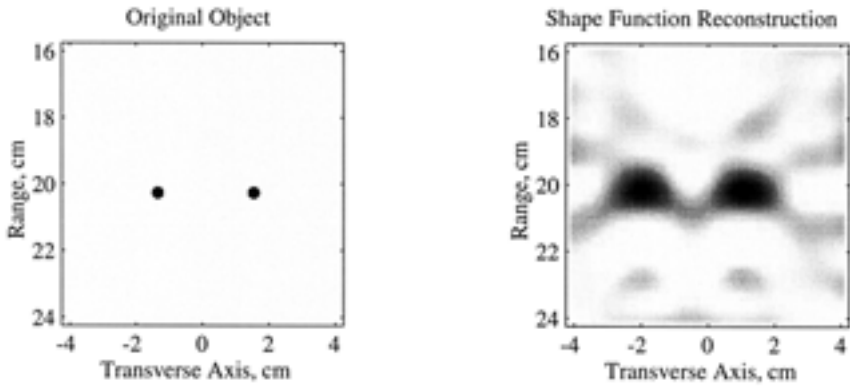
Figure 11. Original object and shape function reconstruction of two metallic cylinders of diameter 4.5 mm aligned horizontally with separation 3.2 cm.
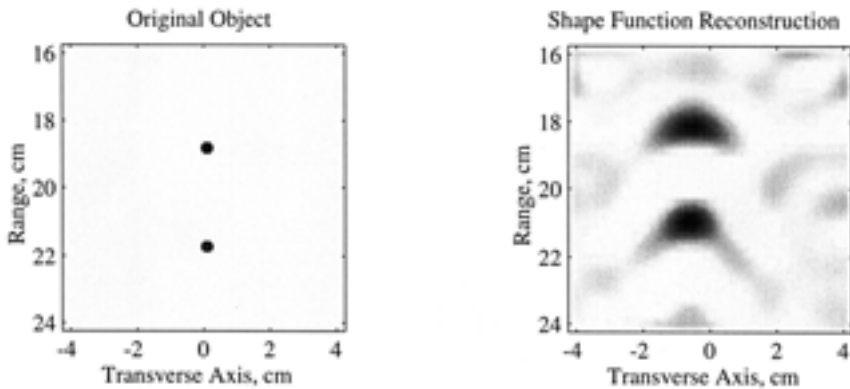

Figure 12. Original object and shape function reconstruction of two metallic cylinders of diameter 4.5 mm aligned vertically with separation 3.2 cm.

Figure 15 shows a DBIM permittivity reconstruction of an empty glass graduated cylinder of diameter 5.25 cm located in air.
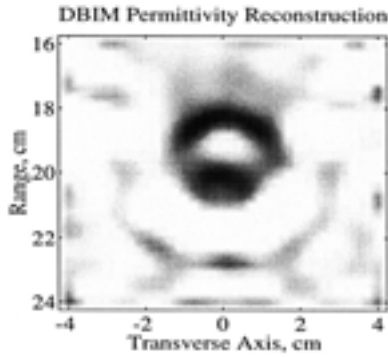
Figure 13. Reconstruction of microwave data from a hollow PVC pipe of diameter 2.7 cm in air.
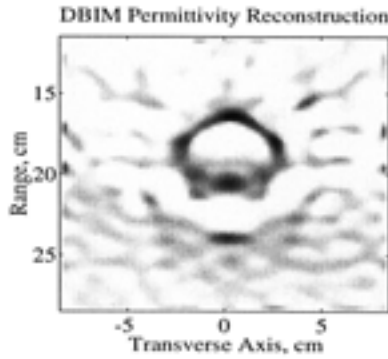
Figure 14. Reconstruction of microwave data from a hollow PVC pipe of diameter 4.8 cm in air.
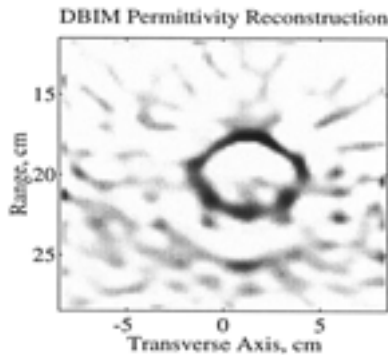

Figure 15. DBIM permittivity reconstruction of an empty glass graduated cylinder of diameter 5.25 cm located in air.

6. CONCLUSIONS

A prototype step-frequency radar microwave imaging system, complete with data collection, calibration, and inverse scattering imaging software, has been designed and built. This prototype imaging system may be used for various NDE applications, and is particularly useful for materials such as concrete, composites, and plastics, that ultrasound has trouble penetrating. The imaging system may be used, for example, to find pipes, voids, and other defects in concrete walls, tunnels, dams, asphalt pavements, etc. It may also be used to detect delaminations and water contamination in advanced composite materials that are used, for example, in ship hulls, masts, and aircrafts.

The SFR imaging system presented here uses multiple antennas in a bistatic arrangement to collect "multiple views" of the scattering object without motion of the array. The Vivaldi antennas used in the array allowed for fairly broadband transduction, with a directional gain characteristic, in a compact, light-weight package. A microwave network analyzer serves as the backbone of the data collection system, requiring very few specialized components other than the antenna assembly and custom data collection software.

A calibration procedure involving the use of a calibration target was presented to remove pulse distortions due to the antennas as well as transmission lines, connectors, amplifiers and directional couplers. It was shown that the calibration procedure does an excellent job of removing pulse distortions, and allows an accurate prediction of the scattered field pulse shape from arbitrary targets with a FDTD forward modeler.

The operating frequency band of $2\,\text{GHz}$ to $12\,\text{GHz}$ used in our system was chosen for laboratory measurements of test objects in air, and shallow penetration NDE applications. For other applications, the choice of operating frequency would clearly depend on the background medium, the desired depth of investigation, and the required object resolution. The antenna size, and hence operating frequency band of the prototype system presented here could be scaled up or down to meet a desired application.

ACKNOWLEDGMENT

assisted in the design, construction, and testing of the initial Vivaldi antennas.

REFERENCES

1. Weedon, W. H., "Broadband microwave inverse scattering: Theory and experiment," Ph.D. dissertation, University of Illinois at Urbana-Champaign, 1994.
2. Bryant, G. H., *Principles of Microwave Measurements,* Peter Peregrinus Ltd., London, 1988.
3. Landt, J. A., "Typical time domain measurement configurations," *Time Domain Measurements in Electromagnetics,* (E. K. Miller, ed.), Van Nostrand Reinhold, New York, 1986.
4. Lawton, R., S. Riad, and J. Andrews, "Pulse & time-domain measurements," *Proc. IEEE,* Vol. 74, 77–81, 1986.
5. Weedon, W. H., and W. C. Chew, "Time-domain inverse scattering using the local shape function (LSF) method," *Inverse Probl.,* Vol. 9, 551–564, 1993.
6. Moghaddam, M., "Forward and inverse scattering problems in the time domain," Ph.D. dissertation, University of Illinois at Urbana-Champaign, 1991.
7. Moghaddam, M., W. C. Chew, and M. Oristaglio, "Comparison of the Born iterative method and Tarantola's method for an electromagnetic time-domain inverse problem," *Int. J. Imaging Syst. Technol.,* Vol. 3, 318–333, 1991.

8. Moghaddam, M., and W. C. Chew, "Nonlinear two-dimensional velocity profile inversion using time domain data," IEEE Trans. Geosci. Remote Sensing, Vol. 30, Jan. 1992.

9. Moghaddam, M., and W. C. Chew, "Study of some practical issues in inversion with the Born iterative method using time-domain data," *IEEE Trans. Antennas Propagat.,* Vol. 41, No. 2, 177–184, 1993.

10. Tarantola, A., "The seismic reflection inverse problem," in *Inverse Problems of Acoustic and Elastic Waves,* (F. Santosa, Y. H. Pao, W. Symes, and C. Holland, eds.), SIAM, Philadelphia, 1984.

11. Devaney, A. J., "A filtered backpropagation algorithm for diffraction tomography," *Ultrason. Imaging,* Vol. 4, 336–360, 1982.

12. Devaney, A. J., "A computer simulation study of diffraction tomography," *IEEE Trans. Biomed. Eng.,* Vol. BME-30, 377–386, 1983.

13. Kak, A. C., "Computerized tomography with x-ray, emission and ultrasound sources," *Proc. IEEE,* Vol. 67, No. 9, 1245–1272, 1979.

14. Broquetas, A., J. Romeu, J. M. Rius, A. R. Elias-Fuste, A. Cardama, and L. Jofre, "Cylindrical geometry: A further step in active microwave tomography," *IEEE Trans. Microwave Theory Tech.,* Vol. 39, 836–844, May 1991.

15. Chew, W. C., *Waves and Fields in Inhomogeneous Media,* Van Nostrand, New York, 1990.

16. Chew, W. C., and Y. M. Wang, "Reconstruction of two-dimensional permittivity distribution using the distorted Born iterative method," *IEEE Trans. Medical Imag.,* Vol. 9, No. 2, 218–225, 1990.

17. Kleinman, R. E., and P. M. van den Berg, "Nonlinearized approach to profile inversion," *Int. J. Imaging Syst. Technol.,* Vol. 2, 119–126, 1990.

18. Joachimowicz, N., C. Pichot, and J.-P. Hugonin, "Inverse scattering: an iterative numerical method for electromagnetic imaging," *IEEE Trans. Antennas Propagat.,* Vol. AP-39, No. 12, 1742–1752, 1991.

19. Chew, W. C., and G. P. Otto, "Microwave imaging of multiple conducting cylinders using local shape functions," *IEEE Microwave Guided Wave Lett.,* Vol. 2, 284–286, July 1992.

20. Otto, G. P., and W. C. Chew, "Microwave inverse scattering-local shape function imaging for improved resolution of strong scatterers," *IEEE Trans. Microwave Theory Tech.,* Vol. 42, No. 1, 137–141, 1994.

21. Caorsi, S., S. Ciaramella, G. L. Gragnani, and M. Pastorino, "On the use of regularization techniques in numerical inverse-scattering solutions for microwave imaging applications," *IEEE Trans. Microwave Theory Tech.,* Vol. 43, 632–640, March 1995.

22. Gibson, P. J., "The Vivaldi aerial," in *Ninth European Microwave Conference,* Brighton, U.K., 1979.

23. Frantz, K., and P. E. Mayes, "Broadband feeds for Vivaldi antennas," *Proceedings of the Antenna Applications Symposium,* University of Illinois, Urbana, September 1987.

24. Sengupta, D. L., and J. E. Ferris, "Rudimentary horn antenna," *IEEE Trans. Antennas Propagat.,* Vol. AP-19, January 1971.

25. Yngvesson, K. S., D. H. Schaubert, T. L. Korzeniowski, E. L. Kollberg, T. Thungren, and J. F. Johansson, "Endfire tapered slot antennas on dielectric substrates," *IEEE Trans. Antennas Propagat.,* Vol. AP-33, December 1985.